RSC Advances

PAPER

View Article Online
View Journal | View Issue

CrossMark click for updates

Cite this: *RSC Adv.*, 2017, **7**, 10564

A general strategy for controllable synthesis of $Ba_3(MO_4)_2$:Mn^{5+} (M = V, P) nanoparticles

Xiaowen Zhang, Yang Li, Zhongliang Hu, Zhi Chen and Jianrong Qiu*

Received 15th December 2016
Accepted 17th January 2017

DOI: 10.1039/c6ra28225c

rsc.li/rsc-advances

The second near-infrared window (NIR-II, 1000–1400 nm) is ideal for fluorescence imaging owing to negligible tissue scattering and minimal autofluorescence. NIR-II luminescence nanophosphors are promising materials for fluorescence imaging. Mn^{5+} is emerging as a new luminescent indicator owing to its typical NIR-I (800 nm) to NIR-II (1190 nm) downconversion luminescence. Herein, we report a facile synthesis approach to prepare Mn^{5+} doped $Ba_3(MO_4)_2$ (M = V, P) nanoparticles with a remarkably sharp emission peak around 1190 nm in the NIR-II region for the first time to our knowledge. The developed two-step approach based on efficient anion exchange reaction is able to not only stabilize the valence but also keep the controlled morphology and uniform size. It is highly possible that the general approach will provide a new perspective on synthesizing special valence ion doped nanosized materials.

Open Access Article. Published on 08 February 2017. Downloaded on 11/24/2024 9:29:02 PM.
This article is licensed under a Creative Commons Attribution 3.0 Unported Licence.

1. Introduction

Recently, a large amount of attention has been devoted to the investigation of fluorescence imaging, which provides visible information about disease with high sensitivity and fast feedback.[1,2] Biological tissues such as skin and blood scatter and absorb less near-infrared (NIR) light than visible light so that the light in the NIR biological window can penetrate these tissues more efficiently.[3] In the past years, extensive investigation has been focused on fluorescent probes emitting in the conventional near-infrared biological window (NIR-I, wavelength of 700–1000 nm).[4–6] Recently, it has been demonstrated that the phosphors for emission in the second near-infrared biological window (NIR-II, wavelength of 1000–1400 nm) and excitation in the NIR-I are optimal for the fluorescence imaging of live animals owing to their lower background noise, greater tissue penetration depth, and reduced photon scattering and photo damage effects.[7,8] Therefore, they are expected to become more desirable in biological imaging. Up to now, numerous bioluminescence probes emitting in the NIR-II region have been developed, such as quantum dots,[9] carbon nanotubes,[10] and lanthanide doped nanomaterials.[11] However, most of those probes suffer from poor photostability, short luminescence lifetime, poor biocompatibility, high toxicity and even high cost.[12] Therefore, their further application is still limited and it is desirable to develop a novel NIR-II luminescence probe for fluorescence imaging.

Mn^{5+}, a transition-metal ion with $3d^2$ electron configuration, is stabilized in a tetrahedral coordination environment, where it has the ^1E state below the $^3T_2$ state, giving rise to a longer-lived NIR emission in the 1000–1400 nm region.[13] Mn^{5+} doped phosphate and vanadate are considered promising candidates for solid-state lasers owing to their long fluorescence lifetime, the strong absorption and effective stimulated emission cross section in the near-infrared region.[14–16] These unique optical characteristics also enable Mn^{5+} doped vanadate and phosphate as potentially ideal bio-probes. So far, there still have been no reports about the application of these materials in fluorescence imaging because not only is Mn^{5+} rare but also Mn^{5+} doped nanosized materials are difficult to synthesize through traditional chemical routes. Mn^{5+} is an unstable ion and valence reduction often occurs during synthesis in aqueous solution, resulting in the formation of undesired MnO_2 precipitate. Although doping with Mn^{5+} has been achieved through solid-state reaction under atmosphere control in previous studies,[17] it is still impractical to control the particle size and morphology *via* this route. In addition, high reaction temperature and long reaction time are required in the whole preparation process. To the best of our knowledge, nanosized materials with Mn^{5+} as the fluorescence center have never been reported. Therefore, it is highly desirable to develop a general but low-cost route to fabricate Mn^{5+} doped nanoparticles.

In this work, we demonstrate a strategy to fabricate for the first time, we believe, Mn^{5+} doped $Ba_3(MO_4)_2$ (M = V, P) nanoparticles in order to achieve fluorescence imaging. $Ba_3(VO_4)_2$:Mn^{5+} nanoparticles with stable valence and controlled size were first successfully synthesized by a convenient two-step method, which not only diminishes the reaction time, but also high reaction temperature and oxygen atmosphere are not required. Stabilized Mn^{5+} ion was obtained through redox reaction in H_2O_2/K_2MnO_4 solution. We also demonstrate that the method is general to the synthesis of other Mn^{5+} doped phosphors such

State Key Laboratory of Luminescent Materials and Devices, Institute of Optical Communication Materials, School of Materials Science and Engineering, South China University of Technology, Guangzhou 510640, P. R. China. E-mail: qjr@scut.edu.cn; Fax: +86-20-87114204; Tel: +86-20-87113646

This journal is © The Royal Society of Chemistry 2017

Open Access Article. Published on 08 February 2017. Downloaded on 11/24/2024 9:29:02 PM.
This article is licensed under a Creative Commons Attribution 3.0 Unported Licence.

as $Ba_3(PO_4)_2$:Mn^{5+} and $BaSO_4$:Mn^{5+}. The luminescence properties, the crystalline structure and the element composition of Mn^{5+} ions in $Ba_3(VO_4)_2$ nanoparticles have been investigated. The strategy based on anion exchange reaction is discussed in detail. Moreover, we made a simple demonstration of $Ba_3(PO_4)_2$:Mn^{5+} for potential application in fluorescent imaging.

2. Experimental section

2.1 Synthesis of undoped $Ba_3(VO_4)_2$ nanoparticles

Undoped $Ba_3(VO_4)_2$ nanoparticles were synthesized by the hydrothermal method. In a typical procedure, 0.8 mmol barium chloride ($BaCl_2$) and 1.6 mmol sodium citrate were dissolved in 40 mL distilled water to form a clear liquid. Then, 1.2 mmol sodium orthovanadate ($Na_3VO_4 \cdot 12H_2O$) was slowly added to the above reaction liquid and precipitated precursor of $Ba_3(VO_4)_2$ appeared. The mixture was stirred for 10 minutes at room temperature. After that, the turbid liquid was transferred into a 50 mL Teflon-lined stainless steel autoclave and treated at 140 °C for 24 h. After the mixture fully cooled down to room temperature, the precipitate was collected by centrifugation at 8000 rpm for 5 min. The as-prepared powder was washed with distilled water and ethanol three times and dried at 60 °C for 6 h in an oven. All the above chemicals were purchased from the Aladdin Chemical Reagent Company, and used as received without any further purification.

2.2 Preparation of manganate(v) solution

Typically, potassium permanganate ($KMnO_4$) was added to a highly alkaline solution (5–10 M KOH) at room temperature and stirred for 12–24 h to form a stable aqueous solution of manganate(VI). Manganate(V) solution was prepared by adding a theoretical amount of 0.1 wt% hydrogen peroxide (H_2O_2) to an ice-cold solution of manganate(VI) in 10 M KOH under vigorous stirring for 1 h and this was followed by filtering to remove MnO_2 precipitate. The color of the solution gradually changed from dark green to sky blue, indicating MnO_4^{3-} was fully generated.

2.3 Synthesis of Mn^{5+} doped $Ba_3(VO_4)_2$ nanoparticles

An anion exchange approach was employed for the synthesis of $Ba_3(VO_4)_2$:1 mol% Mn^{5+} nanoparticles as an example. Typically, 0.10 g of $Ba_3(VO_4)_2$ powder was first dissolved in 5 mL distilled water. Then, 0.16 mL of the 0.01 M K_3MnO_4 solution was added to the obtained solution under vigorous stirring for 15 min. The solution gradually changed color from blue to colorless, indicating a decrease of Mn^{5+} concentration in the solution. The precipitate was collected by centrifugation at 8000 rpm for 5 min and washed with distilled water and ethanol three times. The final purified products were dried under vacuum. $Ba_3(PO_4)_2$:Mn^{5+} was also prepared by the same method.

2.4 Characterization

Powder X-ray diffraction (XRD) was performed on an X'Pert PRO X-ray diffractometer (PANalytical, The Netherlands) using Cu Kα (λ = 1.5418 Å) radiation. The excitation and emission spectra decay curves were measured using a spectrofluorometer (iHR 320, Jobin-Yvon, France) equipped with a 150 W xenon lamp, a monochromator and a liquid nitrogen-cooled DSS-IGA020L InGaAs detector (800–1600 nm). All spectra were corrected for the optical system responses. Thermogravimetric analysis (TG) and differential scanning calorimetry (DSC) were carried out using a thermal analyzer (NETZSCH, STA449C, Germany). The samples were heated at a rate of 10 °C min^{-1} in nitrogen atmosphere. The particle size and distribution of samples were determined by dynamic light scattering (DLS) using an electrophoretic light scattering spectrophotometer (Malvern Instruments Ltd, Zetasizer Nano-ZS, UK). The Raman spectrum was measured with a Raman spectrometer (Renishaw inVia, UK) using a 532 nm laser as an excitation source. The doping concentration of Mn^{5+} was measured by atomic absorption spectroscopy (AAS). A high-resolution transmission electron microscope (HR-TEM, 2100F, JEOL, Japan) was employed to measure the size and morphology of all the samples. Scanning electron microscopy (SEM) images were taken with a field-emission scanning electron microscope (Nova NanoSEM 430, FEI, The Netherlands). Luminescence tissue imaging was performed with a modified imaging system including a Germany pro camera as the signal collector. All luminescence images were taken in a dark room and analyzed with home-made software. An 808 nm laser (LEO, China) was selected as excitation source. Pork tissue samples were purchased from a local market and placed in a dark room kept at 25 °C. All the measurements were carried out at room temperature.

3. Results and discussion

Fig. 1 schematically shows an illustration of the chemical transform approach for synthesizing Mn^{5+} doped $Ba_3(VO_4)_2$ nanoparticles. The main difficulty in the synthesis procedure is to obtain stabilized Mn^{5+} ions. In the first step, 0.1 wt% H_2O_2 solution is employed to effectively reduce Mn^{6+} to Mn^{5+} in our system. The ice-cold H_2O_2/KOH solution offers an alkaline environment to prevent Mn^{5+} being reduced to Mn^{4+}. Subsequently, the undoped $Ba_3(VO_4)_2$ nanoparticles are dissolved in a small volume of KOH/K_3MnO_4 solution under vigorous stirring to form a muddy mixture, where VO_4^{3-} ions are partially replaced by MnO_4^{3-} ions. Finally, the product powder is isolated by centrifugation and washed with ethanol and distilled water. In our experiment, the expected doping concentration of Mn^{5+} is designed to be 0.1, 0.5, 1, 1.5 and 2 mol%. According to the compositional analyses by means of AAS, the evaluated

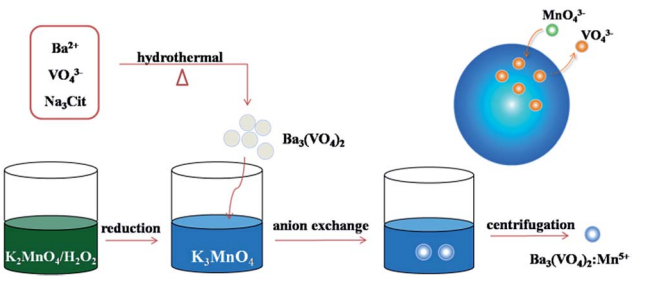

Fig. 1 Schematic illustration of anion exchange procedure for synthesizing Mn^{5+} doped $Ba_3(VO_4)_2$ nanoparticles.

Open Access Article. Published on 08 February 2017. Downloaded on 11/24/2024 9:29:02 PM.
This article is licensed under a Creative Commons Attribution 3.0 Unported Licence.

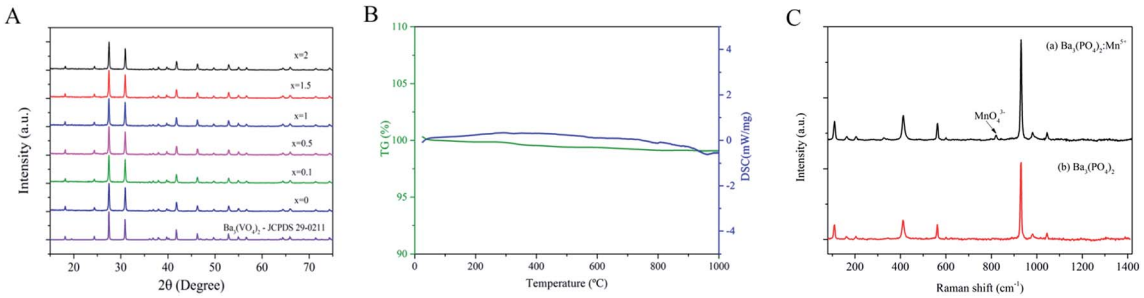

Fig. 2 (A) XRD spectra of $Ba_3(VO_4)_2$:x mol% Mn^{5+} (x = 0, 0.1, 0.5, 1, 1.5, 2); (B) TG and DSC curves of $Ba_3(VO_4)_2$:Mn^{5+}; (C) Raman spectra of (a) $Ba_3(PO_4)_2$:Mn^{5+} and (b) $Ba_3(PO_4)_2$. a.u., arbitrary units.

doping concentrations of Mn^{5+} were 0.021, 0.072, 0.124, 0.361, 0.542 mol%. This reveals that the Mn^{5+} in the solution can only partially be doped into the $Ba_3(VO_4)_2$ host.

Fig. 2A presents the XRD pattern of the $Ba_3(VO_4)_2$:x mol% Mn^{5+} nanoparticles (x = 0, 0.1, 0.5, 1, 1.5, 2). All the diffraction peaks can be well indexed to the standard PDF card (JCPDS no. 29-0211) of rhombohedral phase ($R\bar{3}m$) $Ba_3(VO_4)_2$. The sharp diffraction peaks show that single-phase product with high crystallinity can be obtained by this method. With increasing doping amount of Mn^{5+}, no obvious changes or other detectable Mn impurity were observed, indicating that the occupation of Mn^{5+} did not change the crystal structure of $Ba_3(VO_4)_2$. Fig. 2B shows the TG and DSC curves of $Ba_3(VO_4)_2$:Mn^{5+}. The product exhibits good thermal stability and less mass loss is observed. The result indicates that the nanoparticles have few organic compounds outside. Fig. 2C presents the Raman spectra of undoped $Ba_3(PO_4)_2$ and $Ba_3(PO_4)_2$:Mn^{5+} excited at 532 nm. The Raman signal from MnO_4^{3-} is completely covered by the signal from VO_4^{3-} so that the vibration modes of MnO_4^{3-} are hardly detected in $Ba_3(VO_4)_2$:Mn^{5+}. As a consequence, we use $Ba_3(PO_4)_2$:Mn^{5+} as example. As shown in Fig. 2C, we observe a group of Raman peaks at 112, 406, 562, 931, 983 and 1043 cm^{-1} in undoped $Ba_3(PO_4)_2$ and $Ba_3(PO_4)_2$:Mn^{5+}, which can be attributed to stretching and bending of PO_4^{3-}. The weak Raman peaks at 818 cm^{-1} indicated by an arrow can be attributed to the vibration modes of MnO_4^{3-}.[18]

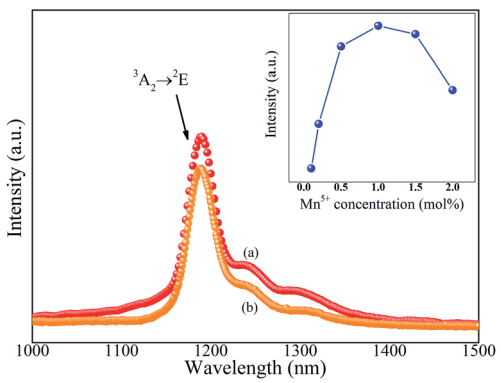

Fig. 3 NIR emission spectra of (a) $Ba_3(VO_4)_2$:Mn^{5+} and (b) $Ba_3(PO_4)_2$:Mn^{5+} phosphors under 808 nm excitation. Inset: concentration dependence of NIR emission intensity of $Ba_3(VO_4)_2$:Mn^{5+} phosphor. a.u., arbitrary units.

Fig. 3 shows the NIR emission spectra of $Ba_3(MO_4)_2$ (M = V, P) nanoparticles at room temperature. Under 808 nm excitation, both of the samples exhibit a sharp emission band at 1190 nm originating from $^1E \rightarrow {}^3A_2$ transition of Mn^{5+} ions. In addition, the two vibronic emission bands centered at 1250 nm and 1300 nm are also detected, which can be assigned to the vibronic transitions of the ν_1(E) and ν_2(A) modes, respectively, of MnO_4^{3-}.[19] It appears that the line shape and luminescence center of $Ba_3(PO_4)_2$:Mn^{5+} are quite similar to those of $Ba_3(VO_4)_2$:Mn^{5+} because Mn^{5+} in tetrahedral coordination has the ^1E state below the $^3T_2$ state, so that the spin-forbidden emission is weakly dependent on crystal field strength.[20] Furthermore, the concentration dependence of emission intensity at 1190 nm for $Ba_3(M_xV_{1-x}O_4)_2$ is given in the inset. The intensity increases with increasing Mn^{5+} doping concentration and reaches a saturation point at x = 0.1, then the intensity begins to decrease with further increasing Mn^{5+} doping concentration owing to the concentration quenching effect.

The photoluminescence excitation (PLE) and photoluminescence (PL) spectra of $Ba_3(VO_4)_2$:Mn^{5+} and $BaSO_4$:Mn^{6+} phosphor are shown in Fig. 4A. By monitoring at λ_{em} = 1080 nm, $BaSO_4$:Mn^{6+} in Fig. 4A(a) exhibits a relatively intense excitation band from 450 to 650 nm and a weak excitation band centered at 750 nm, which can be attributed to the charge transfer transition and $^2T \rightarrow {}^2E$ transition, respectively, of Mn^{6+} ions. The PLE spectrum of $Ba_3(VO_4)_2$:Mn^{5+} in Fig. 4A(b) obtained by monitoring at 1190 nm covers a broad spectral region from 500 to 850 nm and consists of three main excitation bands originating from the d–d transitions of Mn^{5+} ions, including the broad excitation band ranging from 650 to 750 nm assigned to $^3T_1$ to $^3A_2$ transition, the 770 nm band originating from $^3A_2$ to $^1A_1$ transition and the 850 nm band originating from $^3A_2$ to $^3T_2$ transition. In addition, the broad excitation before 350 nm is due to charge transfer transition between O^{2-} and Mn^{5+} ions. In our previous study, $BaSO_4$:Mn^{6+} was considered a promising fluorescent probe because it can offer a broad emission ranging from 900 to 1400 nm, which covers the entire NIR-II biological window. However, most excitation bands of Mn^{6+} ions are in the visible region. In contrast, $Ba_3(VO_4)_2$:Mn^{5+} extends the excitation band into the NIR region, realizing an efficient NIR-I (800 nm) to NIR-II (1190 nm) downconversion luminescence, which has a better performance in biological imaging.

 This journal is © The Royal Society of Chemistry 2017

Open Access Article. Published on 08 February 2017. Downloaded on 11/24/2024 9:29:02 PM.
This article is licensed under a Creative Commons Attribution 3.0 Unported Licence.

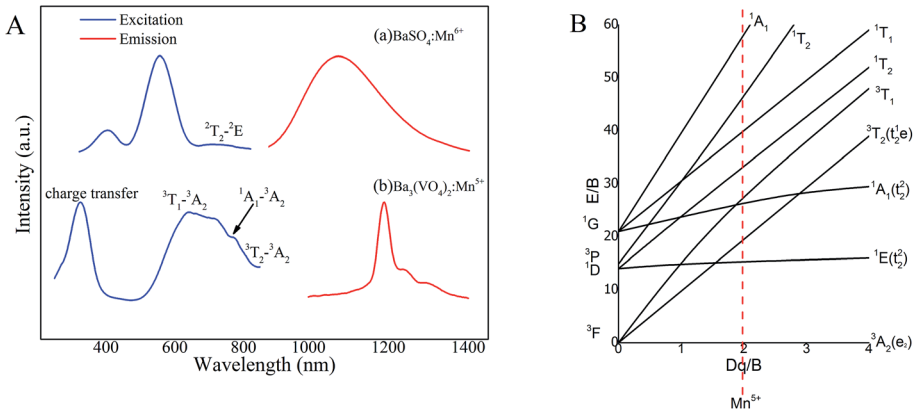

Fig. 4 (A) Photoluminescence excitation and photoluminescence spectra of (a) $BaSO_4:Mn^{6+}$ and (b) $Ba_3(VO_4)_2:Mn^{5+}$; (B) Tanabe–Sugano energy diagram of a $3d^2$ system in a tetrahedral crystal field of Mn^{5+}. a.u., arbitrary units.

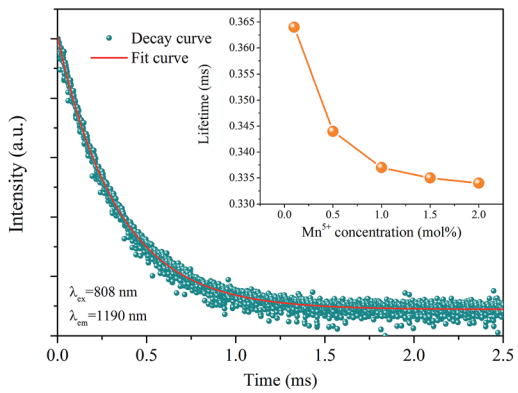

Fig. 5 Decay curve of $Ba_3(VO_4)_2:Mn^{5+}$ phosphor. The red curve is a fit of the experimental data to a single exponential decay equation. Inset: the concentration dependence of fluorescence lifetime of $Ba_3(VO_4)_2$:*x* mol% Mn^{5+} phosphor ($x = 0.1, 0.5, 1, 1.5, 2$). a.u., arbitrary units.

The energy levels of $Ba_3(VO_4)_2:Mn^{5+}$ can be expressed by a Tanabe–Sugano energy level diagram of a $3d^2$ system in tetrahedral crystal field, as shown in Fig. 4B. According to crystal field theory, the energy level sequence of Mn^{5+} ion in tetrahedral environment should be $^3A_2 < {}^1E < {}^1A_1 < {}^3T_2$.[16,21] The $^1E \rightarrow {}^3A_2$ transition of Mn^{5+} ions is not sensitive to local coordination because in a strong field situation, the ground state is a spin triplet $^3A_2$ level and the ^1E level is below the $^3T_2$ level, becoming the first excited state. Based on the Tanabe–Sugano energy level diagram, the photoluminescence process can be described as follows. Firstly, the ground-state electrons of Mn^{5+} ions are promoted to the $^3T_1$, $^1A_1$ or $^3T_2$ level after appropriate light excitation. Then, the excited electrons will relax to the lower ^1E level, giving rise to a longer-lived NIR emission due to $^1E \rightarrow {}^3A_2$ transition.

Fig. 5 exhibits the luminescence decay curves of $Ba_3(VO_4)_2:Mn^{5+}$ excited at 808 nm and monitored at 1190 nm. The red curve is a fit of the experimental data to a single exponential decay equation. The concentration dependence of the fluorescence lifetime of $Ba_3(VO_4)_2:Mn^{5+}$ phosphors is given in the inset. It is found that the decay lifetime is well fitted by a first-order exponential equation:

$$I(t) = I_0 + A\exp(-t/\tau) \quad (1)$$

where $I(t)$ and I_0 represent the emission intensity at times t and 0, respectively. A is a constant and τ is the decay time. The fitted decay times are calculated to be 0.364, 0.344, 0.337, 0.334 and 0.332 ms for $x = 0.1, 0.5, 1, 1.5$ and 2, respectively. It is widely

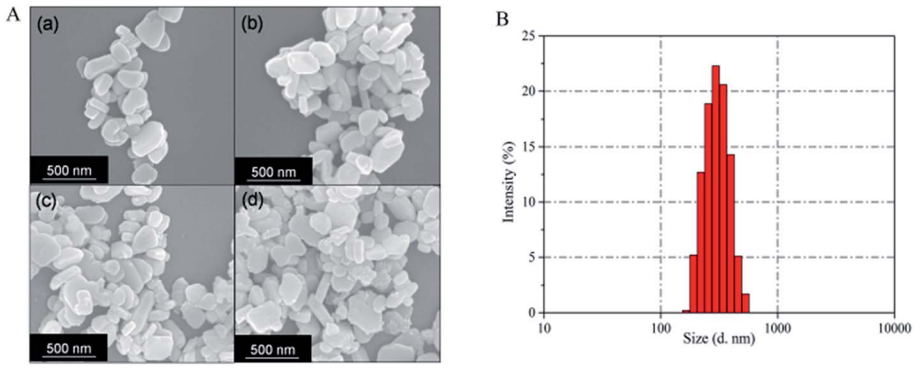

Fig. 6 (A) SEM image of $Ba_3(VO_4)_2$:*x* mol% Mn^{5+} nanoparticles: (a) $x = 0$, (b) $x = 0.5$, (c) $x = 1$, (d) $x = 2$. (B) Particle size distribution of $Ba_3(VO_4)_2$:1 mol% Mn^{5+} nanoparticles, as measured by DLS.

Open Access Article. Published on 08 February 2017. Downloaded on 11/24/2024 9:29:02 PM.
This article is licensed under a Creative Commons Attribution 3.0 Unported Licence.

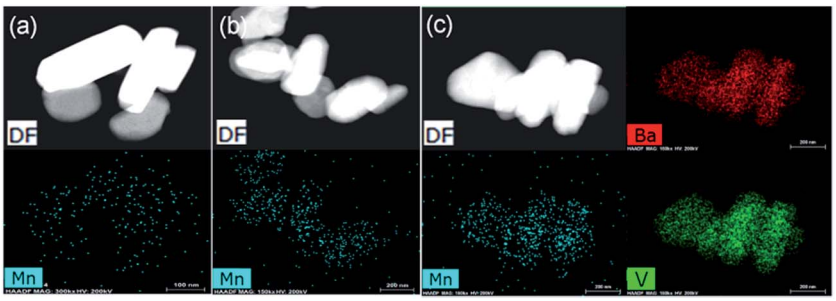

Fig. 7 EDX mapping of $Ba_3(VO_4)_2$:*x* mol% Mn^{5+} with different doping concentrations: (a) $x = 0.5$, (b) $x = 1$, (c) $x = 1.5$. DF, dark field image.

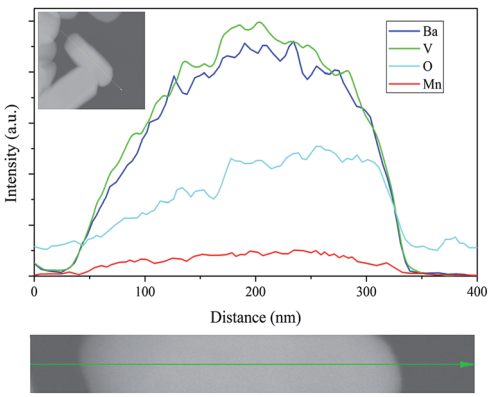

Fig. 8 EDX line scanning of $Ba_3(VO_4)_2$:Mn^{5+}, green, blue and red colors represent V, Ba and Mn elements, respectively. a.u., arbitrary units.

accepted that when Mn^{5+} doping concentration increases, the Mn^{5+}–Mn^{5+} distance decreases, which increases the probability of energy transfer between Mn^{5+} ions and energy transfer to traps or quenching sites. As a consequence, the lifetime is shortened as Mn^{5+} concentration increases.

Fig. 6A presents SEM images of $Ba_3(VO_4)_2$:Mn^{5+} nanoparticles before and after anion exchange reaction. The $Ba_3(VO_4)_2$:Mn^{5+} nanoparticles exhibit flake-like micromorphology with a particle size in the range 150–450 nm. The shape and size of particles remain unchanged after anion exchange reaction at low doping concentration. Fig. 6B shows the particle size distribution of $Ba_3(VO_4)_2$:1 mol% Mn^{5+} nanoparticles, measured by DLS. The mean particle diameter is 295 nm, which corresponds to that in the SEM images. In order to further confirm Mn^{5+} was successfully doped into the $Ba_3(VO_4)_2$ nanoparticles, we carried out elemental mapping measurements and elemental line scanning.

Fig. 7a–c shows the EDX mapping of $Ba_3(VO_4)_2$:*x* mol% Mn^{5+} with different doping concentrations ($x = 0.5$, 1, 1.5). The white color represents the digital TEM image of $Ba_3(VO_4)_2$ nanoparticles. The green, blue and red colors represent V, Mn and Ba elements, respectively. As we can see, Mn^{5+} is distributed uniformly across the nanoparticles. With increasing Mn^{5+} doping concentration, the signal intensity of Mn element becomes higher. A similar result was also obtained in the EDX line scanning of $Ba_3(VO_4)_2$:Mn^{5+}, as shown in Fig. 8. The EDX analysis reveals that the elemental composition of the nanoparticles is Ba, V, O, and Mn. The signal intensity of Mn element distributed at the edges of particles is much lower than that in the center, indicating that the majority of Mn^{5+} ions are distributed on the surface of the nanoparticles. The results demonstrate that Mn^{5+} ions are successfully doped into the $Ba_3(VO_4)_2$ nanoparticles by the chemical transform approach.

In consideration of the similar valence and effective ionic radius, Mn^{5+} ions prefer to occupy the V^{5+} sites in the host. The overall chemical reaction of $Ba_3(VO_4)_2$:Mn^{5+} can be represented by the following equation:

$$x{MnO_4}^{3-} + Ba_3(VO_4)_2 \rightarrow Ba_3(V_{1-x}Mn_xO_4)_2 + (1-x){VO_4}^{3-} \quad (2)$$

Generally, the diffusion rate in ion exchange reaction is an important factor to control the formation of the particles.[22] In bulk materials, the diffusion rates of exchanged ions are quite low owing to the larger particle size. When it comes to nano-sized materials, it has been reported that the diffusion rates are millions of times faster than in the bulk materials.[23] However, anions have larger ionic radius than cations, so that the anion exchange reaction usually has a lower diffusion rate, which always makes rigorous reaction conditions necessary. It is acknowledged that the faster diffusion of cations than

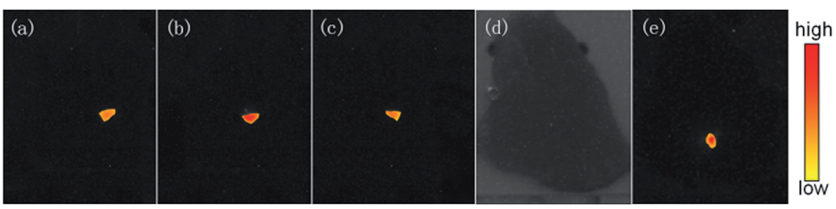

Fig. 9 NIR emission CCD pictures of the $Ba_3(VO_4)_2$:*x* mol% Mn^{5+} nanoparticles with doping concentration at (a) $x = 0.5$, (b) $x = 1$, (c) $x = 1.5$. (d) Optical and (e) fluorescence images of $Ba_3(VO_4)_2$:1 mol% Mn^{5+} nanoparticles in pork tissue, excited by 808 nm laser.

This journal is © The Royal Society of Chemistry 2017

Open Access Article. Published on 08 February 2017. Downloaded on 11/24/2024 9:29:02 PM.
This article is licensed under a Creative Commons Attribution 3.0 Unported Licence.

incoming anions based on the nanoscale Kirkendall effect is the main mechanism to explain the reaction of anion exchange.[24] The nanoscale reduces the reaction barrier of nucleation so that Ba^{2+} are inclined to diffuse outward to the surface of particles and meet with the incoming MnO_4^{3-} ions, leading to the precipitation of Mn^{5+} doped $Ba_3(VO_4)_2$ nanoparticles. The doping concentration of incoming MnO_4^{3-} ions is too low to change the rigid framework of VO_4^{3-} anionic groups. Hence, the initial shape and size of particles is unchanged after reaction.

NIR emission charge-coupled device (CCD) images of the $Ba_3(VO_4)_2$:*x* mol% Mn^{5+} nanoparticles with doping concentrations at $x = 0.5$, 1, 1.5 are given in Fig. 9a–c; these images were obtained by using an AsGaIn camera in a dark room. An 808 nm continuous-wave (CW) laser was used as the excitation source, in combination with a long pass optical filter with a 1000 nm cut-off wavelength. It was clearly observed that the $Ba_3(VO_4)_2$:Mn^{5+} emits intense NIR-I to NIR-II light, indicating the nanoparticles can be effectively excited by an 808 nm laser. To further demonstrate whether the intensity of emission from the $Ba_3(VO_4)_2$:Mn^{5+} is high enough for fluorescence imaging, we have obtained tissue images by injecting the nanoparticles into pork tissue at a depth of 5 mm. Fig. 9d and e show, respectively, optical and fluorescence images of $Ba_3(VO_4)_2$:1 mol% Mn^{5+} nanoparticles in pork tissue under 808 nm laser light. As shown in Fig. 9e, clear high-contrast NIR luminescence with no autofluorescence can be detected with an excitation power density of approximately 500 mW cm^{-2}, suggesting that the novel Mn^{5+} doped nanoparticles are potentially an ideal fluorescent probe in the NIR-II biological window.

4. Conclusions

In conclusion, we provide, for the first time, we believe, a facile two-step strategy based on efficient anion exchange reaction to fabricate Mn^{5+} doped nanoparticles. This novel approach not only can stabilize the valence, but also is able to control the uniform size. The Mn^{5+} doped $Ba_3(MO_4)_2$ (M = V, P) nanoparticles exhibit a remarkable NIR-II emission around 1190 nm with a broad excitation band in the visible and NIR region, which indicates Mn^{5+} doping has potential application in advanced NIR-II fluorescence imaging. By our approach, other candidate hosts for Mn^{5+} ions, consisting of $Ca_3(VO_4)_2$, $Sr_3(VO_4)_2$ and Ba_2SiO_4, can also be fabricated. To sum up, the general strategy illustrated in this paper will likely stimulate new ideas to prepare special valence ion doped nanosized materials.

Acknowledgements

This work was financially supported by the National Natural Science Foundation of China (Grants no. 51472091), Guangdong Natural Science Foundation (Grants no. S2011030001349).

References

1 R. Wang and F. Zhang, *J. Mater. Chem. B*, 2014, **2**, 2422–2443.
2 M. Chen and M. Yin, *Prog. Polym. Sci.*, 2013, **39**, 365–395.
3 A. M. Smith, M. C. Mancini and S. Nie, *Nat. Nanotechnol.*, 2009, **4**, 710–711.
4 V. J. Pansare, S. Hejazi, W. J. Faenza and R. K. Prud'Homme, *Chem. Mater.*, 2012, **24**, 812–827.
5 W. W. Yu, Y. A. W. And and X. Peng, *Chem. Mater.*, 2003, **15**, 4300–4308.
6 J. Chen, C. Guo, M. Wang, L. Huang, L. Wang, C. Mi, J. Li, X. Fang, C. Mao and S. Xu, *J. Mater. Chem.*, 2011, **21**, 2632–2638.
7 G. Hong, J. T. Robinson, Y. Zhang, S. Diao, A. L. Antaris, Q. Wang and H. Dai, *Angew. Chem.*, 2012, **51**, 9818–9821.
8 J. T. Robinson, G. Hong, Y. Liang, B. Zhang, O. K. Yaghi and H. Dai, *J. Am. Chem. Soc.*, 2012, **134**, 10664–10669.
9 Y. Zhang, G. Hong, Y. Zhang, G. Chen, F. Li, H. Dai and Q. Wang, *ACS Nano*, 2012, **6**, 3695–3702.
10 J. T. Robinson, K. Welsher, S. M. Tabakman, S. P. Sherlock, H. Wang, R. Luong and H. Dai, *Nano Res.*, 2010, **3**, 779–793.
11 U. Rocha, K. U. Kumar, C. Jacinto, I. Villa, F. Sanz-Rodríguez, A. Juarranz, E. Carrasco, F. C. J. M. V. Veggel and E. Bovero, *Small*, 2014, **10**, 1141–1154.
12 Y. T. Lim, S. Kim, A. Nakayama, N. E. Stott, M. G. Bawendi and J. V. Frangioni, *Mol. Imaging*, 2003, **2**, 50–64.
13 U. Oetliker, M. Herren, H. U. Güdel, U. Kesper, C. Albrecht and D. Reinen, *J. Chem. Phys.*, 1994, **100**, 8656–8665.
14 L. D. Merkle, A. Pinto, H. R. Verdún and B. Mcintosh, *Appl. Phys. Lett.*, 1992, **61**, 2386–2388.
15 M. F. Hazenkamp, H. U. Güdel, S. Kück, G. Huber, W. Rauw and D. Reinen, *Chem. Phys. Lett.*, 1997, **265**, 264–270.
16 R. Moncorgé, H. Manaa and G. Boulon, *Opt. Mater.*, 1994, **4**, 139–151.
17 T. C. Brunold, M. F. Hazenkamp and H. U. Guedel, *J. Am. Chem. Soc.*, 2002, **117**, 5598–5599.
18 R. Cao, J. Qiu, X. Yu and X. Sun, *ECS J. Solid State Sci. Technol.*, 2013, **2**, R237–R240.
19 L. C. Ferracin, M. R. Davolos and L. A. O. Nunes, *J. Lumin.*, 1997, **72–74**, 185–187.
20 M. Herren, T. Riedener, H. U. Güdel, C. Albrecht, U. Kaschuba and D. Reinen, *J. Lumin.*, 1992, **53**, 452–456.
21 J. A. Capobianco, G. Cormier, M. Bettinelli, R. Moncorgé and H. Manaa, *J. Lumin.*, 1992, **54**, 325.
22 R. D. Robinson, B. Sadtler, D. O. Demchenko, C. K. Erdonmez, L. W. Wang and A. P. Alivisatos, *Science*, 2007, **317**, 355–358.
23 C. Dong and F. C. J. M. V. Veggel, *ACS Nano*, 2009, **3**, 123–130.
24 J. Park, H. Zheng, Y. W. Jun and A. P. Alivisatos, *J. Am. Chem. Soc.*, 2009, **131**, 13943–13945.